

See discussions, stats, and author profiles for this publication at: <https://www.researchgate.net/publication/38036346>

# Pathways of Energy Flow in LHCII from Two-Dimensional Electronic Spectroscopy

ARTICLE *in* THE JOURNAL OF PHYSICAL CHEMISTRY B · NOVEMBER 2009

Impact Factor: 3.3 · DOI: 10.1021/jp9066586 · Source: PubMed

---

CITATIONS

90

READS

28

## 8 AUTHORS, INCLUDING:



Matteo Ballottari

University of Verona

41 PUBLICATIONS 1,846 CITATIONS

[SEE PROFILE](#)



Roberto Bassi

University of Verona

267 PUBLICATIONS 12,832 CITATIONS

[SEE PROFILE](#)



Rienk van Grondelle

VU University Amsterdam

647 PUBLICATIONS 23,715 CITATIONS

[SEE PROFILE](#)

## Pathways of Energy Flow in LHCII from Two-Dimensional Electronic Spectroscopy

Gabriela S. Schlau-Cohen,<sup>†,‡</sup> Tessa R. Calhoun,<sup>†,‡</sup> Naomi S. Ginsberg,<sup>†,‡</sup> Elizabeth L. Read,<sup>†,‡,§</sup>  
Matteo Ballottari,<sup>||</sup> Roberto Bassi,<sup>||</sup> Rienk van Grondelle,<sup>⊥</sup> and Graham R. Fleming<sup>\*,†,‡</sup>

Department of Chemistry, University of California, Berkeley, California 94720, Physical Biosciences Division, Lawrence Berkeley National Laboratory, Berkeley, California 94720, Dipartimento di Biotecnologie, Facoltà di Scienze, Università di Verona, Strada Le Grazie, I-37134 Verona, Italia, and Department of Biophysics, Division of Physics and Astronomy, Faculty of Sciences, Vrije University Amsterdam, NL-1081 HV Amsterdam, The Netherlands

Received: July 14, 2009; Revised Manuscript Received: September 17, 2009

Photosynthetic light-harvesting complexes absorb energy and guide photoexcitations to reaction centers with speed and efficacy that produce near-perfect efficiency. Light harvesting complex II (LHCII) is the most abundant light-harvesting complex and is responsible for absorbing the majority of light energy in plants. We apply two-dimensional electronic spectroscopy to examine energy flow in LHCII. This technique allows for direct mapping of excitation energy pathways as a function of absorption and emission wavelength. The experimental and theoretical results reveal that excitation energy transfers through the complex on three time scales: previously unobserved sub-100 fs relaxation through spatially overlapping states, several hundred femtosecond transfer between nearby chlorophylls, and picosecond energy transfer steps between layers of pigments. All energy is observed to collect into the energetically lowest and most delocalized states, which serve as exit sites. We examine the angular distribution of optimal energy transfer produced by this delocalized electronic structure and discuss how it facilitates the exit step in which the energy moves from LHCII to other complexes toward the reaction center.

### Introduction

Photosynthesis, the process by which plants and bacteria harvest light energy and convert it to chemical energy, fuels most life on Earth. In the initial steps of photosynthesis, pigment protein complexes (PPCs) complete the light-to-charge separation steps with a near unity quantum efficiency. Photosynthetic light harvesting systems function by having a large array of dedicated light-harvesting pigments that absorb energy and funnel the excitation to the reaction center. In the reaction center, the excitation drives a charge separation that begins the photosynthetic chemical reactions.<sup>1</sup> The light-harvesting pigments are grouped locally into complexes with highly specific arrangements within a protein matrix. In higher plants, the majority of photoabsorption occurs in a single type of PPC, light harvesting complex II (LHCII). Over 50% of plant chlorophylls are bound into this complex.<sup>1</sup> LHCII absorbs in a broad spectral region and then directs the photoexcitation to an exit site. From the exit states, the energy traverses across other LHCIIIs and minor light-harvesting complexes toward the reaction center.<sup>1,2</sup>

A full understanding of how LHCII harvests light and directs the photoenergy requires identifying the energy flow pathways as dictated by the proximity and orientation of the pigments and relative energies at which they absorb. In LHCII, the excitation travels from higher energy into lower energy states to the exit site and then transfers from the low energy states to

nearby complexes. The chromophores are all held at nonequivalent sites<sup>3</sup> that, along with the distance and relative orientations of the molecules,<sup>4</sup> produce the manifold of delocalized excited state wave functions. The spatial overlap and energy gaps between these states give rise to the dynamical behavior of the complex. Examining how the structure of the complex produces highly efficient directional energy flow provides insight into the design principles employed in achieving the light harvesting functionality.

LHCII is a heterotrimeric system composed of three similar monomeric subunits (LhcB1–3) arranged with C<sub>3v</sub> symmetry. Each monomer contains chromophores embedded in a protein matrix which itself is held within the thylakoid membrane. Recently, the crystal structure of LHCII was solved with 2.72 and 2.5 Å resolution,<sup>5,6</sup> allowing identification of the chlorophyll species and of the orientation of the chromophores within the complex. Figure 1 shows the crystal structure of the trimeric LHCII complex, looking onto the plane of the membrane. Each LHCII monomer contains 14 chlorophyll molecules, 8 of chlorophyll a (Chl-a) and 6 of chlorophyll b (Chl-b), 4 carotenoids, 3 full-transmembrane α-helices, and 2 partial-transmembrane α-helices. Chl-b differs from Chl-a in that it has an additional carbonyl group that yields a higher energy S<sub>0</sub> to S<sub>1</sub> (Q<sub>y</sub>) transition.<sup>1</sup> According to the crystal structure and site specific mutational analysis, the majority of chlorophyll binding sites are specific to a Chl-a or Chl-b molecule, which suggests that the type of molecule plays an integral role in producing the energy transfer pathways.<sup>5,7</sup> The chlorophylls are arranged in two layers, the stromal and luminal layers, so-called because of their orientation in the thylakoid membrane. Figure 2a displays both layers separately with strongly coupled clusters ( $\sim$ 20–100 cm<sup>-1</sup>) of neighboring chlorophylls indicated as described by Novoderezhkin et al.<sup>8</sup> Spectroscopic studies to

\* Corresponding author.

<sup>†</sup> University of California.

<sup>‡</sup> Lawrence Berkeley National Laboratory.

<sup>§</sup> Current Address: Department of Chemical Engineering, Massachusetts Institute of Technology, Cambridge, MA 02139.

<sup>||</sup> Università di Verona.

<sup>⊥</sup> Vrije University Amsterdam.

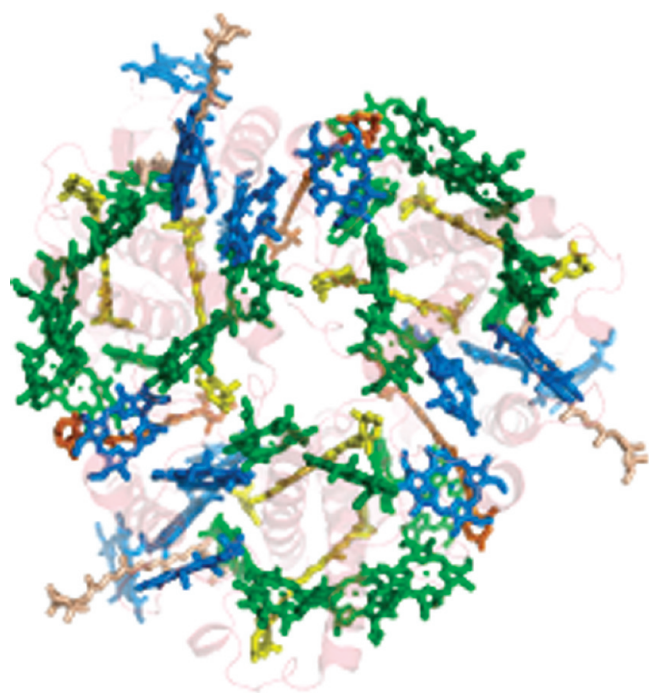


**Figure 1.** Trimeric LHCII complex that consists of pigments (Chl-a in green, Chl-b in blue, carotenoids in orange for violaxanthin, yellow for lutein and off-white for neoxanthin) in a protein matrix.<sup>5</sup>

probe the energies and time scales of energy transfer, when combined with the structural information from crystallography, have the potential to show how the molecular structure gives rise to the electronic structure and the pathways of energy transport.

Components of the pathways of energy transport in LHCII have been mapped using spectroscopic and biochemical tools.<sup>7,9–11</sup> Ultrafast spectroscopic techniques have identified several time scales of energy transfer within the Q<sub>y</sub> excitation region.<sup>10,12–14</sup> LHCII gives rise to a highly congested spectrum such that multiple time scales appear in features at the same energies due to contributions from different chlorophylls. That is, there are similar energy gaps but different energy transfer rates, perhaps due to different spatial relationships, between states on separate chlorophylls within the complex. Three-pulse photon echo peak shift studies (3PEPS) found Chl-b to Chl-b energy transfer had 300 and 800 fs time scales and Chl-a to Chl-a energy transfer occurred on 350 fs, 3 ps, and 6 ps time scales.<sup>12,14</sup> Chl-b to Chl-a transfer was seen from two distinct groups of Chl-b with several different rates of energy transfer. The higher energy excitons within the Chl-b manifold transferred energy to the Chl-a band with 600 fs and 4 ps time constants and the lower energy excitons of the Chl-b band transferred energy to the Chl-a band with 150 and 600 fs time constants. The region between the Chl-b and Chl-a bands has been examined selectively with pump–probe experiments, and these studies have shown a long-lived intermediate state in the region between the two bands.<sup>10,13</sup> Energy transfer out of this state was found to be almost 2 orders of magnitude slower than the other Chl-b to Chl-a dynamics observed,<sup>10</sup> suggesting a different relative structure of this intermediate state.

The pigment-based origin of some of the oscillator strength at certain energies has been identified by correlating spectral sub-bands with individual binding sites using mutated LHCII complexes.<sup>7,11,15</sup> The spectrum of the mutant lacking the chlorophyll at site a614 identified this chromophore as absorbing primarily in the region between the Chl-a and Chl-b bands.<sup>11</sup>

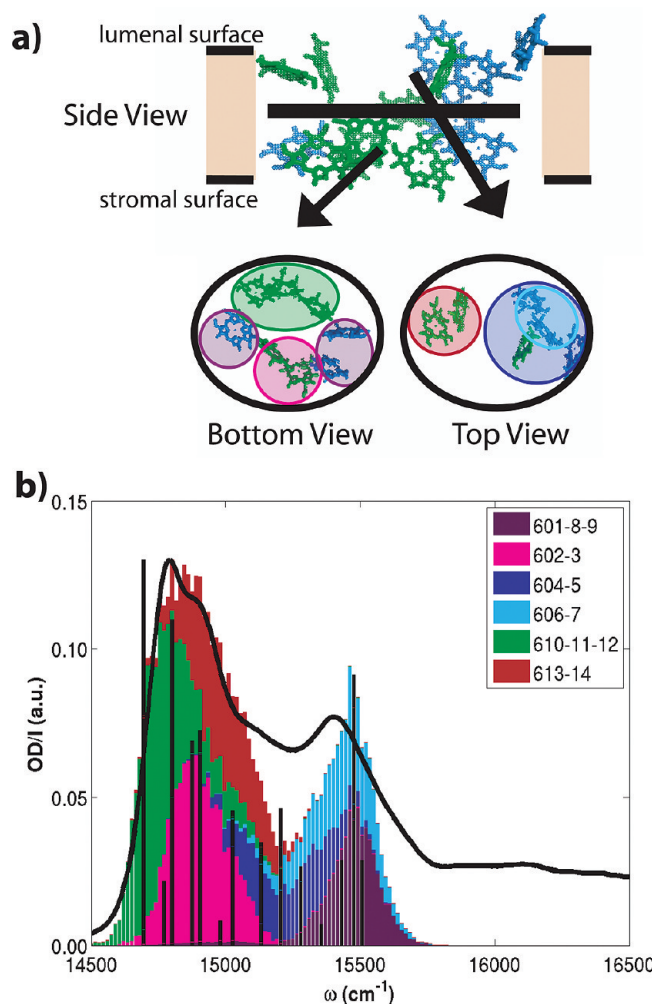


**Figure 2.** (a) Chlorophyll arrangement of monomeric LHCII (Chl-a in green, Chl-b in blue). The strongly coupled clusters within the stromal layer (bottom) and luminal layer (top) are indicated and the color coding corresponds to the spectral regions labeled in b. (b) The linear absorption spectrum of LHCII at 77 K with the calculated site basis contributions averaged over disorder (color) for the excitons (black) plotted. The congested spectrum can be partially decomposed into its site basis contributions by identifying the chlorophylls that absorb in each spectral region (labeled according to the 2.72 Å crystal structure<sup>5</sup>).

The lowest energy portion of the spectrum was found to arise from Chl-a 612 through a mutant lacking this pigment.<sup>11</sup> Additionally, in the spectra from the mutant lacking two of the Chl-a molecules (a611 and a612) from the stromal layer chlorophyll trimer, the red-most region of the Chl-a absorption band was also missing.<sup>7</sup> This suggests that the lowest energy state is located on Chl-a 611 and/or 612, corroborating the finding that the lowest energy oscillator strength is localized on the presumed Chl-a trimer exit site. This result is in agreement with calculations and fitting to results from pump–probe, fluorescence, and linear dichroism experiments,<sup>8,10</sup> all of which were used to produce a Hamiltonian for the complex.<sup>8</sup> Recent low temperature fluorescence and hole burning experiments<sup>16</sup> have also examined the excitonic structure of LHCII. The work of Pieper et al. discussed the possibility of the relative energies of the excitonic states rearranging from 4.2 K to room temperature. The temperature dependence of the structural assignments of the excitonic states is not yet clarified.

The work in this manuscript presents the energy transfer dynamics of LHCII as determined through two-dimensional (2D) electronic spectroscopy over the Q<sub>y</sub> region. The highly congested

linear LHCII spectrum contains closely spaced energy levels, static disorder, and homogeneous broadening, all of which prevent easy identification of energy levels and energy transfer. Our technique extends the emitted signal along a second frequency axis, excitation, which results in displaying the pathways of energy flow. Each 2D spectrum is a frequency-frequency map of absorption, energy transfer, and coupling at a given delay time.<sup>17</sup> The energies of the spectral features correspond to the exciton basis energies, or the eigenvalues of the site basis Hamiltonian. The site basis Hamiltonian has off-diagonal Coulombic coupling terms and diagonal terms consisting of uncoupled transition energies for individual pigments, and so its eigenvectors describe the delocalized excited states of the system, the excitons.<sup>9</sup> In photosynthetic complexes, electronic coupling between nearby molecules based on their relative orientations and proximity within the protein matrix effectively rediagonalizes the system into the exciton basis. It has been shown that the combination of 2D spectroscopic data and theoretical modeling enables the excitons at different energy levels to be mapped back onto the chlorophylls which contribute to those states.<sup>18,19</sup> Using 2D spectroscopy, the relationship between the relative locations of the excited state wave functions and the dynamics of transfer between them can then be elucidated.

An additional question addressed here is how the level of delocalization of excited state wave functions guides energy flow through the complex and creates an effective connection to the rest of the PSII supercomplex. The strength of molecular interaction determines the spatial extent of the wave function. Because spatial overlap facilitates very fast relaxation steps between excited state wave functions and slower steps correspond to traversing larger spatial distances, the physical size of the wave function affects the energy transfer pathways within the complex. The combination of spatial separation and energetic gaps ensures directionality of the energy transfer.<sup>18</sup> Understanding how these optical and dynamical properties arise from a level of delocalization controlled by the specific, finely tuned structural arrangement of chromophores may have applications for designing solar light harvesting devices.

## Methods

**Experimental Methods.** Trimeric LHCII from *Arabidopsis thaliana* was grown and isolated as described by Caffari et al.<sup>20</sup> LHCII was dissolved in 50 mM HEPES buffer (pH 7.6) with the detergent *n*-dodecyl  $\alpha$ -D-maltoside 0.03% and mixed with glycerol at 30:70 (v/v). The sample was sealed in an Oxford Instruments cryostat using a silanized 200  $\mu\text{m}$  quartz cell (Starna). The OD of the sample at 660 nm was measured to be 0.13 (per 200  $\mu\text{m}$ ). To ensure no aggregation occurred at the concentration used, a sample at much lower concentration was prepared as well, and the normalized linear absorption of the two samples were compared to confirm correspondence of all features.

Ultrafast (18 fs) laser pulses centered at 640 nm with 80 nm fwhm were generated in a home-built noncollinear optical parametric amplifier (NOPA). The NOPA was pumped with a home-built Ti:sapphire regenerative amplifier that is seeded by a home-built Ti:sapphire oscillator and that produces a 3.4 kHz pulse train of 45 fs pulses near 800 nm.<sup>21,22</sup> During the experiment, the energy on the sample from each of beams 1, 2, and 3 was 6 nJ per pulse and beam 4 was attenuated, and the beams were focused to a 100  $\mu\text{m}$  beam waist. All measurements were performed at 77 K.

The details of the experimental apparatus, data acquisition, and analysis have been described in detail elsewhere.<sup>21</sup> In brief, the single pulse is split into four with a beamsplitter and a diffractive optic. The use of the diffractive optic allows for phase stability between pulse pairs. Four ultrafast beams are incident on the sample in a so-called box geometry. The signal is generated by the interaction of three of the beams with the sample, causing the signal to emerge in the phase-matched direction,  $k_s = -k_1 + k_2 + k_3$ , collinear with the fourth beam, a local oscillator pulse. The local oscillator is attenuated to ensure it does not interact strongly with the sample. The signal is heterodyne-detected in the frequency domain using spectral interferometry.

The measured electric field is a function of the three time delays between the pulses. The time delay between the first two pulses is known as the coherence time,  $\tau$ , and is controlled to interferometric precision with movable glass wedges, which were scanned from -566.5 to 566.5 fs in 5.5 fs steps. Negative coherence times generate the nonrephasing signal and positive times generate the rephasing signal. Between the second and third pulses, the system evolves dynamically during a so-called "waiting time,"  $T$ . The third time delay, between pulse three and the signal pulse is the rephasing time,  $t$ . The frequency-frequency 2D spectrum at fixed  $T$  is produced by spectrally resolving the signal along  $\omega_t$  and then Fourier-transforming along the coherence time axis,  $\tau$ . In this frequency domain representation, the spectrum directly correlates excitation and emission energies.<sup>21</sup> The ensemble of PPCs evolves in a coherence during both the coherence time and the rephasing time. If the system progresses in conjugate frequencies during these two time periods, this allows for the reversal of dephasing and the generation of a photon echo signal. To produce a nonrephasing signal, the ensemble of PPCs evolves with a phase factor of the same sign during the coherence time and the rephasing time, thus generating a free induction decay signal. The rephasing and nonrephasing signals are separated experimentally by the time ordering of pulses one and two. The signal generated over the entire scan, or the sum of the photon echo and free induction decay contributions, produces a relaxation spectrum. 2D spectra were recorded for waiting times in 10 fs steps from 0 to 500 fs and in 1 ps steps from 1 to 20 ps. Phasing was performed using the projection-slice theorem by separately measuring the spectrally resolved pump-probe (SRPP) signal for each waiting time.<sup>17</sup>

**Theoretical Methods.** The theoretical spectra were generated as described in Zigmantas et al.<sup>19</sup> using nonlinear optical response theory. In brief, a Frenkel exciton model Hamiltonian of monomeric LHCII was used to calculate single and double exciton states. The Hamiltonian was constructed from transition density cube couplings<sup>4</sup> with signs assigned from the ideal dipole approximation (IDA)<sup>8</sup> calculations and site energies determined through fitting to the linear absorption spectrum. Although there may well be mixed binding sites, the structure determined by X-ray crystallography<sup>5,6</sup> is used as a starting point. The site energies were further refined by adjustment of their values to generate simulated 2D spectra that had the strongest agreement with the experimental 2D spectra. The 2D spectra serve as a more sensitive indicator of the accuracy of the fitted transition energies than the linear spectrum. Vibronic transitions on the chlorophylls were not included in the Hamiltonian. The model spectral density included discrete vibrational modes of the bath coupled to the chromophores as previously described.<sup>23</sup> A total of 48 vibrational modes were coupled to the transitions through electron-phonon interaction and weighted according to their Huang-Rhys factors, determined experimentally using fluo-

rescence line narrowing and rescaled to fit the data.<sup>24</sup> Fast nuclear motion contributing to the homogeneous broadening was additionally included in the line shape with a single overdamped Brownian oscillator. Quantum dynamical calculations were performed using modified Redfield theory.<sup>25</sup> The inhomogeneous broadening, or the effects of slow nuclear motion, was described by explicit averaging over a Gaussian distribution around the site transition energy with  $\sigma = 80 \text{ cm}^{-1}$  through 200 realizations.

## Experimental Results

The linear absorption spectrum in the region of the first electronic excited state of the chlorophyll molecules in the LHCII complex is shown in Figure 2b. The combination of the two species of chlorophyll present in LHCII, differences in the local environment of each chromophore within the asymmetric structural motif, and variation in how each pigment couples to its neighbors creates a broadened, highly congested spectrum. The linear absorption spectrum of the Q<sub>y</sub> region shows both Chl-a and Chl-b bands, centered at 14925 and 15385  $\text{cm}^{-1}$ , respectively. The Chl-b peak has a vibronic tail<sup>11,26</sup> on the high energy side of the peak, which also contains a small contribution from the Chl-a S<sub>0</sub> to S<sub>2</sub> (Q<sub>x</sub>) transition.<sup>15</sup>

The real (absorptive) portions of experimental 2D electronic spectra of LHCII are displayed in Figure 3 at waiting times selected to summarize the dynamics of the system. In the relaxation spectra of Figure 3, left, the peaks along the diagonal predominantly correspond to the linear absorption spectrum, with two Chl-a peaks (the main peak and the shoulder peak) at 14775 and 14900  $\text{cm}^{-1}$  and the Chl-b peak at 15400  $\text{cm}^{-1}$ . The energy transfer pathways appear as positive features (cross-peaks) below the diagonal, because energy transfers downhill to the lower energy states. Pronounced excited state absorption (ESA) is seen as a strong negative peak above the diagonal. The intensity of the negative feature arises from the collective oscillator strength of the large manifold of double-exciton states (91 for each monomer).

The relaxation spectra, which display the purely absorptive line shape, are shown next to their corresponding isolated nonrephasing contributions in Figure 3. The nonrephasing spectra display a characteristic “phase-twisted” line shape or mixed absorptive and dispersive character that results in extension in the antidiagonal direction.<sup>27</sup> To identify and isolate the energy transfer cross-peaks, the nonrephasing spectra provide a useful tool because the off-diagonal portion generally contains mostly contributions from energy transfer and ESA, two processes that produce signal fields of opposite sign. Because coherence peaks appear only on the diagonal in the nonrephasing spectra, the off-diagonal region of the nonrephasing spectra lacks the coherent beating characteristic of relaxation or rephasing spectra.<sup>28</sup> Therefore, evolution of positive features off the diagonal results from energy transfer as opposed to coherent beating features.<sup>29</sup>

Energy transfer cross-peaks appear along two discrete values of  $\omega_t$ , corresponding to the two resolved diagonal peaks within the Chl-a band ( $\omega_t = 14775 \text{ cm}^{-1}$ ;  $\omega_t = 14900 \text{ cm}^{-1}$ ). The excitation region can be divided into three main sections: (1) Chl-b ( $\omega_r > 15200 \text{ cm}^{-1}$ ); (2) the range between Chl-a and Chl-b or the intermediate region ( $15000 \text{ cm}^{-1} < \omega_r < 15200 \text{ cm}^{-1}$ ); and (3) Chl-a ( $\omega_r < 15000 \text{ cm}^{-1}$ ), which contains two peaks (midenergy Chl-a and low energy Chl-a). Energy transfers out of these three regions into the states that produce the two Chl-a peaks. This gives rise to five cross-peaks (marked with arrows in Figure 3a–d, right). The major cross-peak on the picosecond time scale is indicated separately as cross-peak 6 (CP6) in Figure 3e. Square regions with a side of 85  $\text{cm}^{-1}$  around each cross-

peak were integrated in the absolute value nonrephasing spectra to elucidate time scales of energy transfer. The absolute value spectra were used for this analysis to eliminate amplitude variations due to uncertainty in the spectral phase. To examine the very fast early time dynamics (up to 300 fs), the normalized peak traces were subtracted from a normalized integrated region around the lowest energy diagonal rephasing signal. The rephasing low energy diagonal peak is invariant with respect to the dynamics of the system; it only evolves with overall signal decay and time-point specific experimental fluctuation. The peak does not decay as population relaxes and coherence pathways appear off the diagonal in rephasing spectra.<sup>28</sup> The subtraction was performed to isolate the dynamical evolution in cross-peak amplitude by removing noise that changes at each time point. The resulting difference traces were smoothed using a five-point moving filter and are plotted in Figure 4a. The slower time scale of the several hundred femtosecond energy transfer processes allows the evolution to be seen directly in the smoothed traces of the integrated regions because the smoothing function does not damp the dynamics. These smoothed integrated regions are plotted in Figure 4b for 360–430 fs. We examine relaxation processes on three distinct time scales: sub-100 fs, several hundred femtoseconds, and over picoseconds. Absorption across all regions shows eventual relaxation to the lowest energy state.

The energy transfer processes within 100 fs seen here show faster dynamics than found in previous experiments<sup>10,12–14</sup> or predicted theoretically.<sup>8</sup> For waiting times of 30 and 70 fs ( $T = 30 \text{ fs}$  and  $T = 70 \text{ fs}$ ), the spectra highlight the appearance and evolution of these ultrafast dynamics. Energy transfer at all five cross-peaks appears around 30 fs. Initially, there is previously unobserved higher relative amplitude of the peaks in the midenergy Chl-a region. These two peaks show energy transfer from the intermediate region, cross-peak 3 (CP3), and the Chl-b region, cross-peak 5 (CP5). By 70 fs, the relative amplitude of the cross-peaks indicating transfer to the low energy Chl-a region is larger. This rise is seen in the increased amplitude of cross-peaks 2 (CP2) and 4 (CP4) in the 70 fs spectrum.

The cross-peak between the midenergy Chl-a region and the lowest energy Chl-a region ( $\omega_r = 14980 \text{ cm}^{-1}$ ;  $\omega_t = 14795 \text{ cm}^{-1}$ ), labeled as cross-peak 1 (CP1) in Figure 3, is directly probed for the first time here. Previous photon echo peak shift experiments<sup>12</sup> monitored population decay as the excitation transferred out of the states encompassed by the limited bandwidth of the laser pulse used. In our 2D data, after the sub-100 fs initial population of this cross-peak, the peak again increases quickly to a maximum at  $\sim 130 \text{ fs}$  and then grows slowly until  $\sim 250$ –300 fs, as shown by the integrated trace of Figure 4a. The slower component is similar to that seen in the transient grating experiments,<sup>12</sup> but the very rapid component has not been observed previously. This is perhaps due to the significantly shorter pulse duration achieved here or the ability to precisely resolve excitation and emission frequencies, thus, better separating this region from other dynamics of the system.

The evolution observed here after  $\sim 100 \text{ fs}$  and over the next several hundred femtoseconds agrees with previous experiments and theoretical predictions.<sup>10</sup> Energy transfer peaks appear from the intermediate region, which lies between the Chl-a and Chl-b bands and so contains contributions from high energy Chl-a and low energy Chl-b. Energy transfer peaks connecting the intermediate region to each band within the main Chl-a region are labeled as CP2 ( $\omega_r = 15100 \text{ cm}^{-1}$ ;  $\omega_t = 14775 \text{ cm}^{-1}$ ) and CP3 ( $\omega_r = 15100 \text{ cm}^{-1}$ ;  $\omega_t = 14900 \text{ cm}^{-1}$ ) in Figures 3 and 4. After the sub 100 fs appearance of these two cross-peaks, a

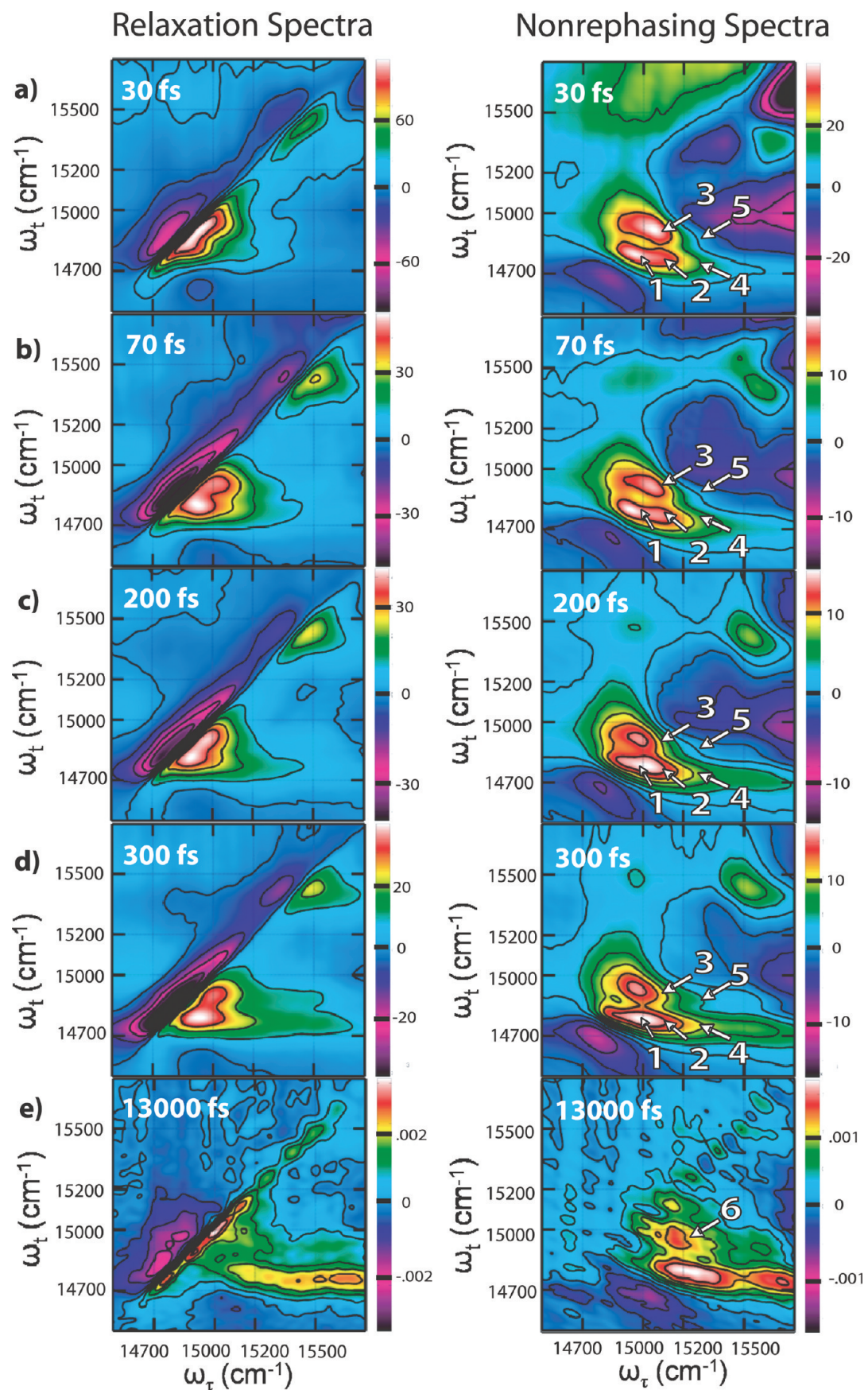


**Figure 3.** Experimental real 2D relaxation (left) and nonrephasing (right) spectra of LHCII at 77 K for  $T = 30, 70, 200, 300$  fs, and 13 ps. Arrows point to cross-peaks on the nonrephasing spectra to highlight energy transfer dynamics and the tick marks as drawn delineate the regions of the spectrum discussed in the text.

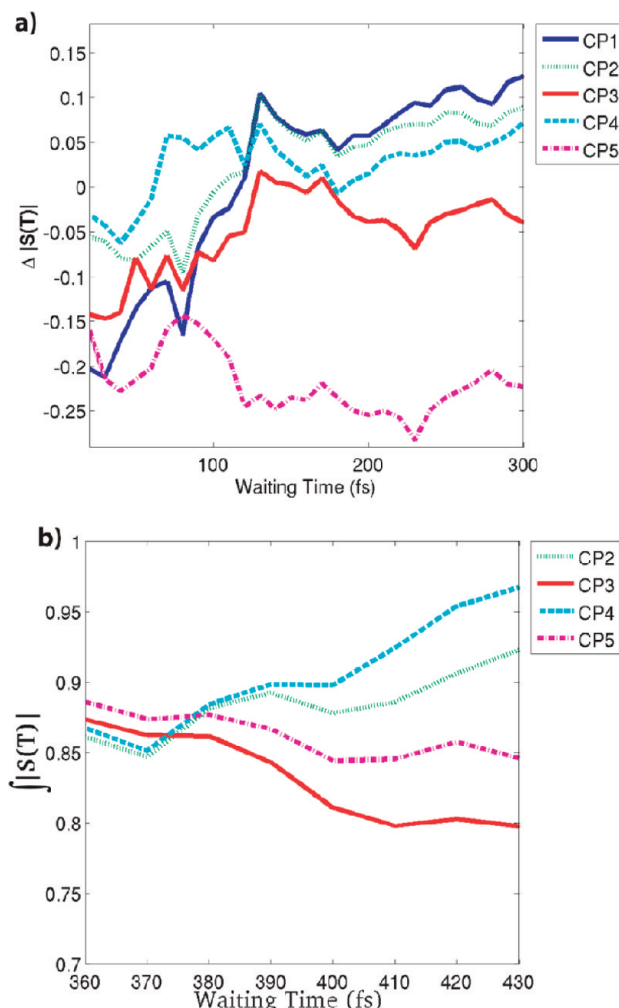


**Figure 4.** (a) Integrated square regions ( $85 \text{ cm}^{-1}$  per side) around each cross-peak are shown for waiting times of 20–300 fs (the 0–20 fs dynamics are not shown because they are dominated by pulse overlap effects). The normalized integrated regions are subtracted from the normalized integrated region around the low energy diagonal rephasing peak to eliminate variations at each population time and then the difference trace is smoothed. The cross-peak numbers are as shown in Figure 3 (CP1: mid Chl-a  $\rightarrow$  low Chl-a; CP2: intermediate region  $\rightarrow$  low Chl-a; CP3: intermediate region  $\rightarrow$  mid Chl-a; CP4: Chl-b  $\rightarrow$  low Chl-a; and CP5: Chl-b  $\rightarrow$  mid Chl-a). (b) The integrated square regions are smoothed and plotted without subtraction for CP2–5. The concomitant decay of CP3 and 5 and rise of CP2 and 4 indicate a multistep relaxation process.

second component of energy transfer from the intermediate region to the midenergy Chl-a region, or CP3, grows between 210 and 280 fs. This is seen most readily in Figure 3c,d, right, where the relative amplitude of CP3 has again increased compared to the peak below it (CP2) from the  $T = 200$  fs spectrum to the  $T = 300$  fs spectrum. CP2, which arises from energy transfer out of the intermediate region to the lowest energy states, rises rapidly to a second maximum at  $\sim 130$  fs, followed by slower growth from  $\sim 150$ – $300$  fs, as seen in the difference trace of Figure 4a. The increased absolute amplitude of CP2 is also seen directly in the  $T = 200$  fs nonrephasing spectrum (Figure 3c, right). CP3 decays after  $\sim 300$  fs, as is seen in the traces of the integrated regions of Figure 4b. CP2 grows in over the same time period, starting at  $\sim 360$  fs. The relative dynamics over 300–500 fs illustrate the correlation between the decrease of CP3 and the increase of CP2, which suggests a multistep mechanism for relaxation into the lowest energy state.

Rapid relaxation within the Chl-b band around  $15400 \text{ cm}^{-1}$  is seen by 70 fs through the asymmetry on the lower right of the Chl-b diagonal band in the relaxation spectra. The antidiagonal broadening characteristic of nonrephasing signals can obscure cross-peaks near the diagonal. In this case, due to the small energy gaps within the Chl-b band, the cross-peaks are more clearly visible in the relaxation spectra than in the nonrephasing spectra, and can be seen in the left-hand column of Figure 3a–d. On the picosecond time scale, the cross-peak is no longer evident as seen in Figure 3e.

Energy transfer from the Chl-b band to the Chl-a band also shows a several hundred femtosecond component. In the  $T = 300$  fs spectrum in Figure 3, the cross-peak showing transfer from the Chl-b region to the midenergy Chl-a region, CP5 ( $\omega_r = 15290 \text{ cm}^{-1}$ ;  $\omega_t = 14880 \text{ cm}^{-1}$ ), has grown in strongly as compared to the  $T = 200$  fs spectrum. Over the next several hundred femtoseconds CP5 slowly decays, as presented in Figure 4b. The cross-peak from the Chl-b band to the low energy Chl-a region, CP4 ( $\omega_r = 15290 \text{ cm}^{-1}$ ;  $\omega_t = 14745 \text{ cm}^{-1}$ ), grows in significantly at  $T = 360$ – $400$  fs. The decay of CP5 begins shortly thereafter. CP4 strengthens further over the next hundred femtoseconds. The relative evolution of these two peaks again demonstrates a multistep relaxation mechanism where Chl-b absorbed energy transfers to the lowest energy state both directly and through midenergy Chl-a states. The integrated regions for these two cross-peaks in Figure 4b and their similarity to the integrated regions for CP2 and CP3 show that there are fairly comparable dynamics for both sets of cross-peaks. In other words, the same multistep relaxation process out of the intermediate region, seen in the anticorrelated behavior of CP2 and CP3, also occurs out of the Chl-b band, seen in the anticorrelated behavior of CP4 and CP5.

Differences in the rates of transfer into the Chl-a band from the intermediate and Chl-b regions can also be seen in the traces of Figure 4. In Figure 4a, the later rise of CP4, as compared to CP2 over the 200–300 fs range, suggests slower transfer from the Chl-b band than from the intermediate region. The slightly earlier decrease of CP3 than CP5 in Figure 4b also indicates faster intermediate region to Chl-a transfer. Although transfer out of the intermediate region and the Chl-b band display similar stepwise relaxation through the Chl-a region, the greater energy gap gives rise to slower transfer from the Chl-b band than from the intermediate region into the midenergy Chl-a peak. While both sets of cross-peaks along the two  $\omega_r$  bands (CP2 and CP4, CP3 and CP5) often exhibit similar dynamics, the differences seen in this stepwise relaxation, as well as in earlier energy transfer times, corroborate the theoretical model which predicts that these regions correspond to separate states and thus display separate dynamics. The differences in their dynamical evolution are also seen clearly in the early time behavior as shown in the traces of Figure 4a.

On the picosecond time scale, a long-lived intermediate state, appearing at the red edge of the Chl-b absorption and indicated as CP6 ( $\omega_r = 15250 \text{ cm}^{-1}$ ;  $\omega_t = 14880 \text{ cm}^{-1}$ ) in Figure 3e, right, shows an alternate pathway of energy transfer from the red edge of the Chl-b band to the Chl-a band. As shown by the decay of CP3 and CP5 in Figure 4b, energy transfers out of the midenergy Chl-a band by 500 fs. At 1 ps, another cross-peak has emerged showing relaxation into a state in the midenergy Chl-a region, the energy remains trapped in this state and the strength of CP6, which is the cross-peak corresponding to this process, decays with the overall signal. All picosecond spectra (1–20 ps) display the same cross-peak, whose only evolution is the overall signal decay. The  $T = 13$  ps spectrum

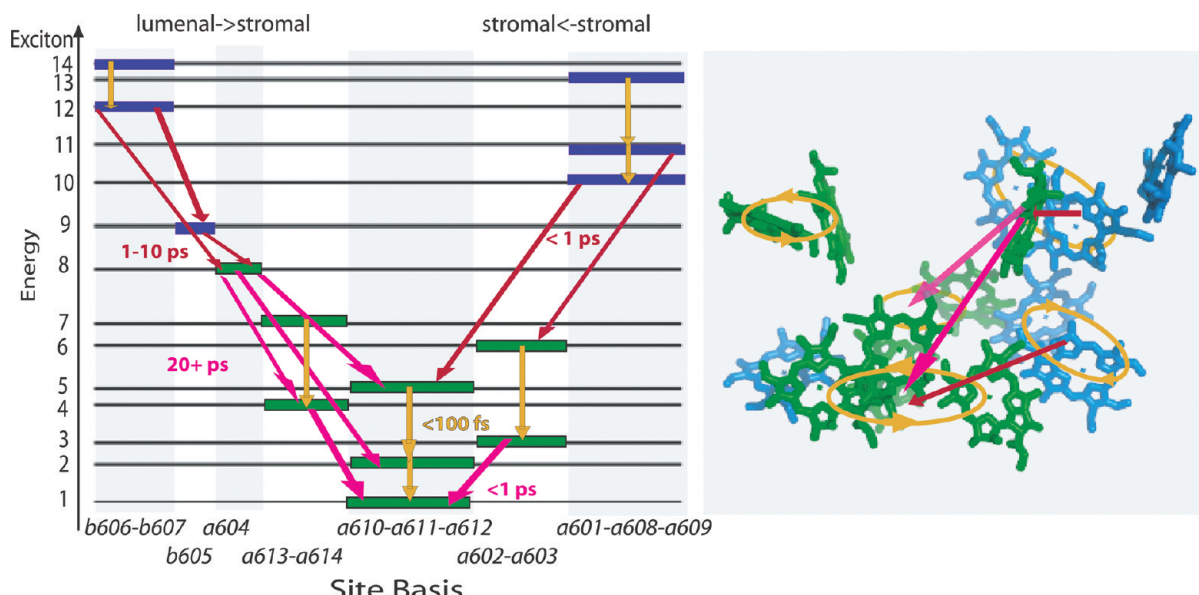


**Figure 5.** Summary of the pathways of energy flow and their locations as mapped onto the crystal structure.<sup>5,10</sup> The major pigments with contributions to each exciton are determined by the working Hamiltonian, and the excitonic energy is found with the electronic coherence beating signal.<sup>30</sup> The time scales indicate the approximate time at which the cross-peak signal corresponding to that pathway reaches its maximum.

is presented as an example to illustrate the intermediate state during this time range. This suggests the existence of access to the lowest energy state via alternate states, in this case most likely a monomeric chlorophyll spatially and energetically separated from the lowest energy states.<sup>8</sup> The location of this molecule could select for distinct energetic transfer pathways, as opposed to a step-down relaxation through all states available in the complex. The excitation is channeled to the low energy state based also on spatial proximity as opposed to simply across the smallest possible energy gap.

## Discussion

We base our discussion of energy relaxation pathways on the Hamiltonian developed here and also on the dynamical modeling of Novoderezhkin et al.,<sup>8</sup> which uses the 2.72 Å LHCII structure of Liu et al.<sup>5</sup> The exciton energies used for analysis are those determined through the coherent beating signal in a recent study,<sup>30</sup> while the pigment participations, and resultant site basis attributions for energy flow, are those from the Hamiltonian developed in this work. This model will be discussed in the theoretical discussion later in this manuscript. We use the monomeric LHCII as a subunit to discuss the absorption and energy transfer dynamics of LHCII. This is a reasonable starting point as only one coupling greater than 10 cm<sup>-1</sup> was calculated between monomers (35.7 cm<sup>-1</sup> between two Chl-b molecules), while within the Q<sub>y</sub> region, strong intramonomeric electronic couplings of over 100 cm<sup>-1</sup> exist.<sup>4</sup> Although neglect of this Chl-b–Chl-b coupling yields a red shift in the exciton energies of the Chl-b band, the strong couplings between Chl-b and Chl-a, and the major Chl-a to Chl-a couplings, are limited to within an individual monomer. Therefore, the Chl-b to Chl-a and Chl-a to Chl-a relaxation pathways are essentially localized on the monomer. In this paper, we confine ourselves, with the exception of a few brief comments, to the dynamics of these relaxation steps. The site basis contributions to each spectral region, grouped into the strongly coupled clusters of chlorophyll as shown in Figure 2a, are averaged over disorder and plotted in Figure 2b. In this figure, the effect of fast nuclear motion on the line shape is only included as a linear shift in transition energies. Although

each pigment contributes to absorption across a range of energies because of both static disorder and participation in multiple excitons, the region at which it absorbs begins to provide a basis for isolating the energy transfer dynamics into the contributions from individual pigments. The energy transfer pathways discussed within the following paragraphs are summarized in Figure 5. The major site basis contributions to each exciton are indicated in the figure. The time scales written indicate the time of the approximate maximum of the amplitude of the portion of the cross-peak corresponding to that energy transfer step.

*Chl-a → Chl-a Energy Transfer.* The electronic coupling between chlorophyll molecules in LHCII is strong enough that most of the exciton states have significant amplitude on two or three chromophores. The strong interaction ( $\sim 20\text{--}100\text{ cm}^{-1}$ ) and consequently significant energetic splitting between the excitons localized within several groups of pigments allow large energy “jumps” by relaxation within an excitonic manifold as was observed (between effective dimer pairs) in the Fenna–Matthews–Olsen (FMO) complex, another photosynthetic complex that has been studied with 2D spectroscopy.<sup>18</sup> In other words, spatial overlap between exciton states is more important in controlling the pathway of energy flow than stepwise transfer down the energetic ladder. For LHCII, the strongly coupled groupings obtained from Novoderezhkin et al.<sup>8</sup> are circled in Figure 2a.

An example of the phenomenon of strong coupling between chlorophylls and the resultant splitting in energy levels allowing large energetic steps in the relaxation pathways is seen in transfer out of the intermediate and midenergy Chl-a region and into the lowest energy excitons in the Chl-a manifold. According to the Hamiltonian used to simulate the spectra, one of the higher energy Chl-a excitons ( $k = 5$ ) is found on the a610–a611–a612 trimer. The pigment-based oscillator strength from the trimer on the high energy side of the Chl-a peak is also shown in Figure 2b with the amplitude in green, and the dynamical relaxation is indicated in Figure 5. The other two exciton levels on the trimer are the two lowest excitons ( $k = 1, 2$ ) of the 14 excitons in the monomeric LHCII model. The large spatial overlap gives rise to fast relaxation between these excitonic states. As seen in Figure 3a and b, CP1 connects the midenergy Chl-a ( $k = 5$ )

with the lower energy portion ( $k = 1, 2$ ) on a sub-100 fs time scale, as expected for processes expedited through spatial overlap. The highest energy exciton ( $k = 5$ ) on the trimer also contributes to the intermediate region in some realizations over static disorder, which would appear as similarly rapid transfer out of the intermediate region to the middle Chl-a (the middle energy exciton on the trimer), CP3, and low energy Chl-a (the lowest energy state), CP2. The rates for one such realization were calculated theoretically by Novoderezhkin et al.<sup>10</sup> The theoretical rate predictions for one typical realization over static disorder produced energy transfer rates between spatially overlapped excitonic states at around 100 fs. In the case of the three excitons localized on the chlorophyll trimer, which in this realization are  $k = 1, 2$ , and 8, the time constants are  $\tau_{8-2} = 90$  fs and  $\tau_{8-1} = 220$  fs. The cross-peaks corresponding to these two pathways would therefore appear in a 2:1 amplitude ratio corresponding reasonably well to the CP3/CP2 amplitude ratio in the 30 fs spectrum.

According to the model for monomeric LHCII, two of the cross-peaks that appear in under 100 fs correspond to transitions within the two excitons on the Chl-a dimers. Based on the exciton energies of the model, the dimer on the stromal level (a602–a603) contributes to CP1, which exhibits energy transfer within 50 fs. The amplitude of this peak continues to increase rapidly until  $\sim 150$  fs. This dimer is more weakly coupled than other clusters ( $17.4 \text{ cm}^{-1}$ ), leading to more localized excitonic states and therefore slower energy transfer than other intracluster relaxation steps. The increase in the amplitude of CP1 between 50–150 fs could arise from the transition on this stromal dimer. According to the model, the site basis transition energies of the luminal dimer (a613–a614) are higher, so relaxation within this dimer would appear in CP3. This cross-peak connects the intermediate and midenergy Chl-a region ( $k = 7$  to  $k = 4$ ) and shows significant amplitude in the 70 fs spectrum. The contribution of Chl 613 and 614 to energy transfer between the intermediate and midenergy Chl-a regions is also consistent with the proposed mixed specificity of these chlorophyll binding sites, with mid- and high-energy Chl-a and low-energy Chl-b.<sup>7</sup> To reduce the complexity of the system we preferred to maintain the Chl-a specificity of the Chl 613 and 614 sites proposed by the crystal structure of LHCII.<sup>5,6</sup> The theoretical calculations of Novoderezhkin et al.<sup>8</sup> predict intradimer energy transfer of  $\tau_{4-2} \approx 300$  fs and  $\tau_{7-3} \approx 150$  fs (for excitons generated in one typical realization over static disorder) for the stromal and luminal dimers, respectively. The ratio of the rates from the spectra is similar to that found theoretically, however, the rates themselves seen experimentally are faster than those predicted or seen with other techniques. The sub-100 fs dynamics found here, which are observable due to the shorter pulse duration in our experiment, are evidence for short-time energy transfer. Previous theoretical investigations lacked the data to which a short-time dynamical model could be matched. The mismatch between the faster rates observed in our experiment and the theoretical simulations could arise from neglect of relaxation between vibronic levels and correlated motion at two or more sites in the protein bath which could contribute to coherence transfer processes.<sup>19</sup>

The next group of energy transfer processes appears over the course of several hundred femtoseconds and is thought to occur between nearby clusters of chlorophylls. CP1, the midenergy Chl-a band transferring to the low energy Chl-a band, shows a slower rise from  $\sim 150$ –250 fs. This likely arises from transfer from the lower energy state of the luminal (higher energy, a613–a614) dimer to the stromal trimer and dimer. CP3, the

intermediate region transferring to the midenergy Chl-a region, also shows an increase from 210–280 fs. In this case, the higher energy exciton on the luminal dimer ( $k = 7$ ) could transfer to the stromal dimer ( $k = 6, 3$ ) and stromal trimer ( $k = 5, 1, 2$ ). Additionally, the complex displays a multistep relaxation that would agree with a relaxation route through the stromal dimer to the stromal trimer. CP2, the intermediate region to low energy Chl-a peak, rises to a maximum at  $\sim 440$  fs, concomitant with the decay of CP3, the intermediate region to the midenergy Chl-a peak.

Greater spatial as well as spectral separation leads to much slower energy transfer mechanisms illustrated by CP6 in Figure 3e. Upon occupation of the model's highest energy Chl-a exciton ( $k = 8$ ), located mostly on a604, the excitation remains in this state for much longer than any other step in the relaxation pathway. Very slow relaxation out of this state to lower energy states in the Chl-a band is seen in the delayed appearance of CP6. Photon echo peak shift experiments by Agarwal et al.<sup>12</sup> also showed a distinctly slower component of Chl-a–Chl-a energy transfer compared to the fast initial energy transfer detected. The slow time scale of this decay was probed directly with TA experiments.<sup>10</sup> The series of 2D spectra clearly shows population continuing into the picosecond region in this long-lived intermediate, or “bottleneck”, state, as illustrated in the  $T = 13$  ps spectrum. Some population remains in the intermediate state as the signal dies at  $T = 20$  ps. These picosecond transitions to lower energy Chl-a excitons ( $k = 1, 2, 3, 6$ ) are also shown in Figure 5. The model of Novoderezhkin predicts slow transfer out of this intermediate state. The exciton predominantly localized on a604 ( $k = 8$ ) is essentially monomeric and the spatial distance to lower energy excitonic wave functions creates a bottleneck state in the model. This step of energy transfer proves to be the slowest step in the relaxation pathways in the complex though the 20 ps extent of the 2D spectroscopy cannot pinpoint the exact decay constant.

*Chl-b → Chl-b Energy Transfer.* The Chl-b exciton levels in the Novoderezhkin et al. model are rather extensively mixed<sup>8</sup> in the highest six excitons, and this produces energetically close states with large spatial overlap, so relaxation between them is very fast (Figure 3a–d, left). The similar rates and spectral congestion preclude more precise identification of different energy transfer pathways. By one picosecond, energy has transferred out of the Chl-b band almost entirely, so that the Chl-b to Chl-b cross-peaks disappear (as seen in the  $T = 13$  ps spectrum in Figure 3e).

*Chl-b → Chl-a Energy Transfer.* The role of excitonic spatial overlap in facilitating relaxation over a large energy gap is also important in explaining Chl-b to Chl-a energy transfer. Because relaxation rates scale with spatial overlap, two distinct pathways between the Chl-b and Chl-a manifolds occur. The structural arrangement of the chromophores into the stromal and luminal layers produces parallel pathways of relaxation located on each of them.

The previously unobserved sub-100 fs component of energy transfer between the Chl-b and Chl-a bands, revealed in the growth of CP4 and CP5 in Figure 3a,b, has several potential contributions. In addition to Chl-b contributions, ultrafast relaxation of Chl-a vibrational states that are similar in energy to Chl-b states could contribute to these cross-peaks as the Chl-a band shape shows a significant vibronic contribution isoenergetic with the Chl-b region.<sup>31</sup> Examining the electronic transitions of the model, the strong Chl-b to Chl-a coupling within the complex results in excitons delocalized over both chlorophyll species. On the luminal level, Chl-a, a604, is coupled to its

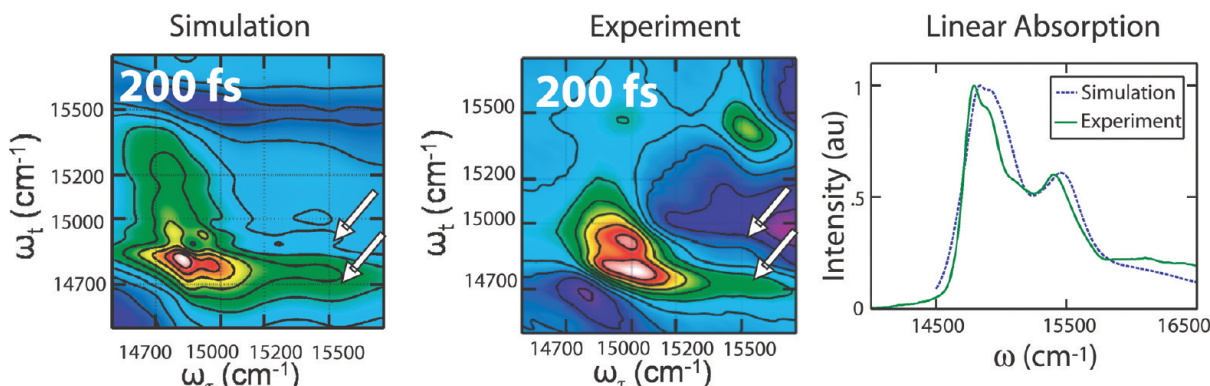


**Figure 6.** LHCII 77K normalized experimental and simulated linear absorption and real nonrephasing 2D electronic spectra shown for  $T = 200$ . Energy transfers from Chl-b and the intermediate region into two distinct Chl-a bands, as indicated with arrows on the spectra. Most population is collected in the lowest state.

neighboring Chl-b, b605. The resultant splitting yields a lower energy exciton ( $k = 8$ ) localized mostly on the Chl-a and a higher energy exciton ( $k = 9$ ) localized mostly on the Chl-b. The spatial overlap from the two delocalized states over the two sites gives rise to fast relaxation over the Chl-b to Chl-a energy gap, which could contribute to the previously unobserved component of energy transfer from Chl-b to the midenergy Chl-a band in the 30 fs spectrum (CP5). In the picosecond spectra (e.g., Figure 3e), CP6, which corresponds to where energy transfer from the other two luminal Chl-b molecules would appear in the model, also emerges clearly once the excitation remains trapped on a Chl-a, a604. The appearance of this cross-peak first in the 1 ps spectrum indicates that some relaxation steps occur on a much longer, or picosecond, time scale.

On the stromal level, another pathway could contribute to the sub 100 fs Chl-b to Chl-a energy transfer. Within 100 fs, CP4, transfer from Chl-b to low energy Chl-a, has weak amplitude. The very rapid dynamics could arise from the strong coupling ( $71.6 \text{ cm}^{-1}$ ) between Chl-b 609 and Chl-a 603. Other Chl-b molecules within the trimer of which b609 is a part are also strongly coupled ( $47 \text{ cm}^{-1}, -21.9 \text{ cm}^{-1}$ ) to the dimer of which a603 is a part. This strong coupling leads to spatial overlap between these two excitonic states and, thus, a potential sub-100 fs relaxation pathway.

The spatial overlap and resulting splitting produces a two step pathway for energy to travel from Chl-b to the exit site. Energy can transfer from the Chl-b bands to the low energy excitons via the higher energy dimer exciton ( $k = 6$ ) or the higher energy trimer exciton ( $k = 5$ ), as shown in Figure 5. Energy transfer into the midenergy Chl-a peak (CP5) reaches a maximum around 290 fs and then decays. One of the things that leads to this decay is transfer out of the midenergy Chl-a band to the lower energy Chl-a states. Concurrent with this decay is the growth of a cross-peak, CP4, between the Chl-b band and the low energy Chl-a, which continues to grow from 350–500 fs (the first part of this process is shown directly in Figure 4b). The energy probably transfers first into the midenergy Chl-a states because of the small energy gap and then exploits the spatial overlap to transfer down to the lowest energy excitons ( $k = 1, 2$ ) in the complex, as mapped out in the discussion of energy transfer within the Chl-a manifold.

**Theoretical Discussion.** In Figure 6, we compare the experimental and calculated nonrephasing spectra at  $T = 200$  fs along with the experimental and calculated linear absorption spectra. In general, the simulated 2D spectra display the features seen in the experimental results, corroborating the working Hamiltonian developed here as representing the electronic

structure reasonably well. The theoretical calculation accurately reproduces the emergence of two distinct cross peaks between the Chl-a and Chl-b bands (CP4 and CP5), clearly showing the relaxation to two separate regions within the Chl-a band. The horizontal band along the lowest energy states in the theoretical spectrum displays transfer into the low energy states from all initially excited levels in accord with experiment. In addition, the experimental multistep relaxation mechanisms within the complex are reproduced theoretically, when the two bands of cross-peaks eventually turn into a single low-energy band. We do, however, see mechanisms on different time scales than in the experimental spectra perhaps due to an inaccurate bath model. Relaxation between vibronic states as well as correlated bath motions are neglected here, though recent work has indicated correlations between the environments of individual binding sites are important in photosynthetic complexes.<sup>32</sup>

The Chl-b band displays significantly less oscillator strength in the simulated nonrephasing spectrum than in the experimental one in Figure 6. Coherence effects appear along the diagonal in nonrephasing spectra, so variations in oscillator strength could result from the weaknesses in the bath model. Additionally, the Chl-b band is red-shifted in the simulated spectra, which has been found previously to arise from neglect of intermonomer coupling.<sup>8</sup> The match in the linear absorption spectra could arise from the long vibronic tail effectively red-shifting the peak of the Chl-b band in the experimental linear data.

Generating simulated spectra which reproduced the experimental results reasonably well required adjusting the site energies from the previously determined model Hamiltonian<sup>8</sup> to better match the data. The new site energies produce two distinct peaks in the Chl-a region, a feature lacking in simulations that use the site energies of ref 7. With the latter model, the  $150 \text{ cm}^{-1}$  energy gap between the two bands within the Chl-a region seen in the 2D spectra was not reproduced in simulations. 2D nonrephasing spectra, in particular, because they show elongation in the antidiagonal direction, allow for easier identification of exciton position and clearer visualization of the double peak structure.

The new site energies can also produce energetically separated excitons located on the same chromophores. These increased intracluster energy gaps also give rise to smaller energy differences between clusters, facilitating cluster-to-cluster transfer. Overall, we see more evenly spaced excitonic energies resulting from greater variation in the site energies used to match the experimental results.<sup>30</sup> Additionally, the resultant excitonic structure contains nearby or overlapping states in different spectral regions causing cross-peaks to emerge very rapidly, as

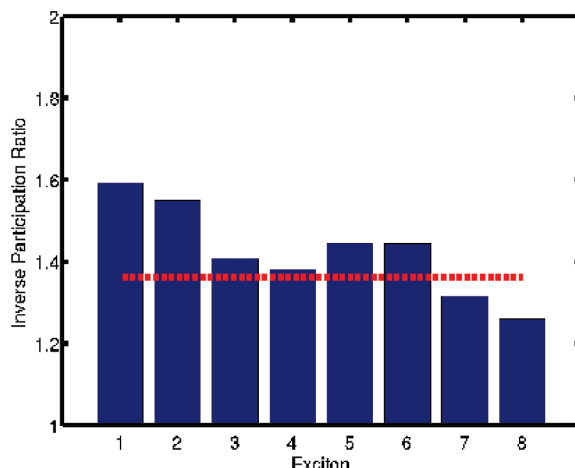


**Figure 7.** Inverse participation ratios of the excitons in the Chl-a region, averaged over 2000 realizations of static disorder, indicate the high level of delocalization of excitons 1 and 2. The average of the inverse participation ratios of the Chl-a excitons without significant contributions from the trimeric exit site is plotted in red.

seen in the dynamics of the experimental spectra. Despite the improvements made here, the limitations in the simulations and the remaining mismatch between the experimental and calculated results indicate that the Hamiltonian requires further refinement.

**Intercomplex Transfer.** It is interesting to compare the low energy states of LHCII and the FMO complex,<sup>10,18</sup> two light harvesting complexes that have been studied in detail by a variety of spectroscopic methods including 2D spectroscopy. The two complexes have rather different functions and this is represented in their excitonic structure. FMO functions as an excitonic wire connecting the chlorosome to the reaction center. The lowest energy state is proximal to the reaction center and is localized on an essentially monomeric exciton (site 3).<sup>18,33</sup> In contrast, LHCII sits in a network of light harvesting complexes comprising the antenna portion of the Photosystem II supercomplex. Its function would not be well served by having the excitation be rapidly focused onto a single Chl-a molecule. On the contrary, by having the lower energy states delocalized over a number of molecules, energy transfer may be facilitated over a broad range of exit directions enabling both LHCII-to-LHCII transfer and LHCII-to-minor complex transfer within the supercomplex. Our analysis shows that this is indeed the case as we now demonstrate.

Figure 7 shows the calculated inverse participation ratio, a measure of excitonic delocalization,<sup>34</sup> averaged over 2000 realizations of static disorder. The figure was generated with the modified Hamiltonian used for the theoretical simulations. The inverse participation ratio ( $P_\alpha^{-1}$ ) of an exciton  $\alpha$  is expressed in terms of its wave function  $\phi_\alpha$ ,

$$P_\alpha^{-1} = \frac{1}{\sum_m |\varphi_\alpha(m)|^4}$$

where  $m$  indexes the site energies.<sup>34</sup> As shown in Figure 7, the two lowest energy excitons are clearly the most delocalized. In a typical single realization over static disorder, excitons 1 and 2 have inverse participation ratios of 2.86 and 2.00, respectively. Proposed intercomplex transfer pathways are located on the trimeric site over which these two excitons are delocalized.<sup>2</sup> For example, in ref 2, Chl-a 612 is found to be ~17 Å from

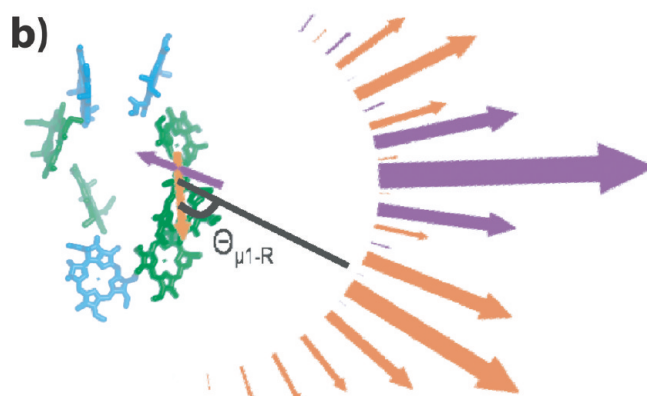
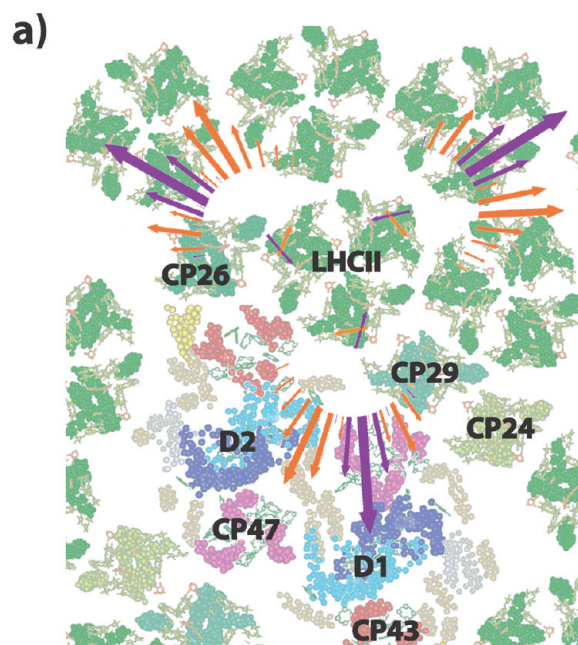


**Figure 8.** (a) Magnitude of the angular contribution to the orientation factor for three monomers in an LHCII trimer is shown for exciton 1 (orange) and exciton 2 (purple) for each angle on a structural model of PSII. The positions and angles of excitons 1 and 2 are displayed on the sample LHCII trimer in the same colors as their corresponding outcoupling factors. The length of the emergent arrows indicates the strength of the factor for the exciton to which its color corresponds integrated over all realistic orientations of the acceptor dipole. (b) Outcoupling factors for an isolated monomer.

Chl 11 of the PSII core complex inner subunit CP43 and Chl-a 610 is also thought to be important in intercomplex energy transfer.<sup>10</sup> The two lowest energy excitons, at  $14700\text{ cm}^{-1}$  and  $14770\text{ cm}^{-1}$ , are separated by an energy gap of less than  $k_B T$  at room temperature.<sup>31</sup> This small energy difference and the large spatial overlap between the states allow for rapid transfer between them. Because both states have non-negligible amplitude on the chlorophylls thought to participate in the exit pathway (the chromophores are located on the external edge of the complex), they can both serve as donors in intercomplex energy transfer.

While the two lowest energy states overlap spatially, they are oriented at different angles in the membrane plane. This angle between them allows for energy transfer from the LHCII exit site in a range of directions and to a range of acceptor state transition dipole angles. Figure 8 shows the donor–acceptor coupling magnitude integrated over all acceptor angles for

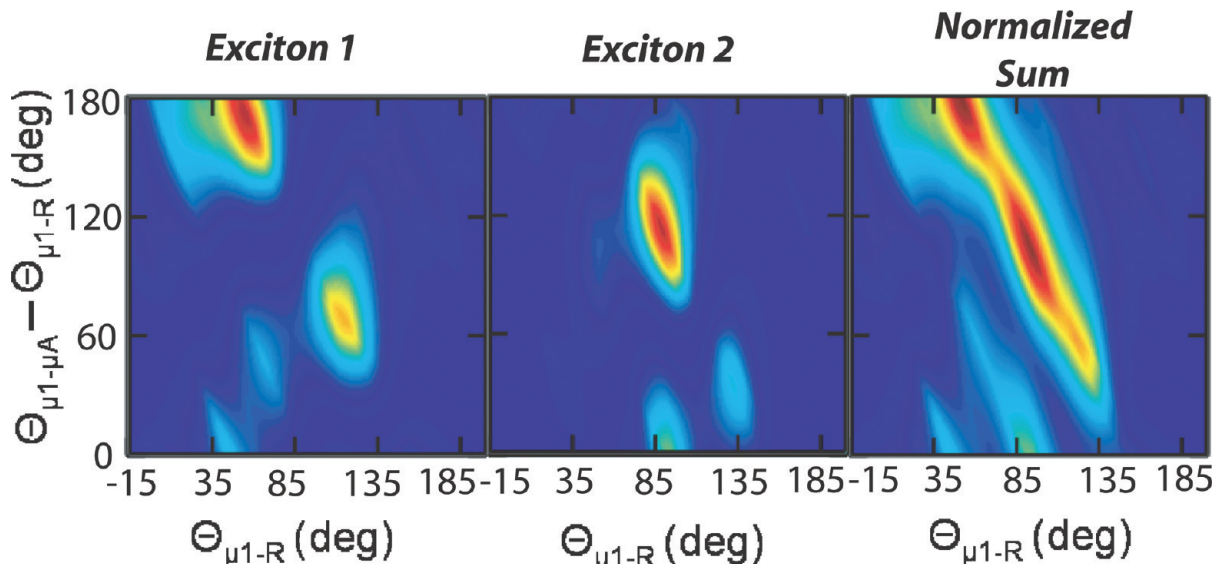


**Figure 9.** Orientational outcoupling factors for energy transfer from excitons 1 and 2 individually and the sum of both normalized contributions are plotted. The values are calculated with the distributed-dipole method. To compare their magnitudes across the range examined for both exciton 1 and exciton 2, they are plotted as a function of the angle between the exciton 1 dipole and the internuclear line and the exciton 1 dipole and the acceptor dipole at a distance of 60 Å. The range was chosen based on likely orientations, as determined by the position of excitons 1 and 2 within the complex.

excitons 1 and 2 directed outward from the exit site. Because the two excitons are optimized for transfer in different directions, together they allow for energy to exit LHCII across a broad distribution of angles. This is ideal for transfer to the various relative positions of nearby complexes, as shown in Figure 8. Energy transfer between complexes can be described by Förster theory when they are separated by a distance larger than the exciton size.<sup>35</sup> The resulting rates depend on a coupling factor based on the relative geometry and distances of the donor and acceptor states. In the case of the LHCII exit site, where the donor–acceptor distance is the same order of magnitude as the extent of the wave function, an accurate description of the coupling factor is given by the potential calculated with the distributed dipole approximation<sup>36</sup>

$$V = \sum_{m,n} \frac{\lambda_m \lambda_n \kappa_{mn} |\vec{\mu}_m| |\vec{\mu}_n|}{r_{mn}^3}$$

where  $m$  and  $n$  are the sites that give rise to the donor and acceptor wave functions, respectively,  $\lambda_m$  is the coefficient corresponding to the contribution for that site to the excitonic wave function, and  $r_{mn}$  is the donor–acceptor distance. A result of this equation is that when two donor excitons have different site basis participations, the coupling factors are optimized for excitation energy transfer in different directions relative to the two donor transition dipoles. This effect comes from the need to look at the distances and relative angles between not only the donor exciton and the acceptor, but also between the site basis contributions to the donor exciton and the acceptor. This is clearly seen in Figure 8. In this equation, the angular dependence is given by  $\kappa_{mn}$ ,

$$\kappa_{mn} = \cos(\theta_{mn}) - 3 \times \cos(\theta_{mr}) \times \cos(\theta_{nr})$$

where  $\theta_{mn}$  is the angle between the transition dipoles of sites  $m$  and  $n$  and  $\theta_{mr}$  is the angle between the transition dipole of site  $m$  and the interchromophore vector between sites  $m$  and  $n$ . For transfer

from site  $m$  of the donor wave function to site  $n$  of the acceptor wave function, the orientational factor can be rewritten as

$$\kappa = \cos(\theta_{\mu_m - \mu_n}) - 3 \times \cos(\theta_{\mu_m - R}) \times \cos(\theta_{\mu_m - R} - \theta_{\mu_m - \mu_n})$$

The distributed dipole coupling factor was calculated for dipoles projected into the membrane plane as a function of radial distribution around the exit site ( $\theta_{\mu_k - R}$ , for exciton  $k$ ) and acceptor angle ( $\theta_{\mu_k - A}$ ) with LHCII exciton 1 as the acceptor. It was assumed that there was no displacement perpendicular to the membrane plane. Because these complexes are held within the thylakoid membrane, the orientational coupling factor was determined as a function of the angle between the exciton  $m$  and acceptor dipoles, calculated for all angles, and the acceptor position, placed 60 Å from the point in between the center of excitons 1 and 2 and scanned for all physically relevant angles. To examine only the angular contributions to the coupling factor, the values from both excitons were normalized and summed. Figure 9 shows the relative strengths of the orientation factors for excitons 1 and 2 for all acceptor angles at each of the internuclear directions and also the sum of the two excitons' contributions. Depending on its placement within the PSII supercomplex, LHCII transfers to other LHCII complexes, to other monomers within the complex, to one of multiple minor complexes, or to core complex inner antenna subunits.<sup>2</sup> As shown in the sum of orientational factor contributions, the delocalized low energy states and resultant two potential donors serve to optimize donor–acceptor overlap across all directions and angles in the membrane plane. From this design, the energy transfer pathway is more robust to variations in acceptor state angle and position.

## Conclusions

2D electronic spectroscopy maps the dynamical behavior of a system as a function of both excitation and emission frequencies. This is particularly useful in examining photosynthetic systems in which the manifold of closely spaced electronic states and broadening through static disorder yield highly

congested spectra. By extending the measured signal into a second frequency dimension, previously unresolved dynamical evolution and peak location are identified. Nonrephasing signals allow further isolation of energy transfer peaks because dynamics of positive, off-diagonal features arise from energy transfer processes without coherent contributions.

The 2D spectra presented here illustrate the pathways along which LHCII, as the major light harvester in plants, collects energy from its pigments. The coupling between the pigments produces delocalized excited state wave functions through which the complex guides energy to exit states, the characteristics of which are optimized for transfer to nearby complexes. Theoretical models of experimental results show that energy transfer from Chl-b to Chl-a occurs first within each layer (luminal and stromal) of chlorophylls and then from the luminal to the stromal layer, where the lowest energy excitonic states are localized. These types of parallel energetic pathways where the complex exploits the spatial overlap of delocalized excited states to relax across large energy gaps has been seen in other photosynthetic complexes<sup>18</sup> and could contribute to the efficiency of photosynthetic energy transfer. The existence of multiple pathways located on different regions of the complex allows for the most direct route to the exit states.

The energy transfer pathways seen here are partially determined by the gradation of site basis transition energies. The Chl-b molecules on the outer edges of the LHCII monomer and the higher energy Chl-a molecules on the luminal layer conduct the excitation to the centrally located, lower energy exit site on the stromal layer. The more evenly spaced manifold of excitonic states produced by the site energy adjustments in this work agrees qualitatively with a recent study in which coherent beating was exploited to determine the exciton energies in LHCII.<sup>30</sup> Furthermore, the work of Müh et al. used *ab initio* calculations to show the ability of the protein matrix to tune the local electric field and, therefore, change the site-basis transition energies for FMO.<sup>37</sup> A similar calculation for the LHCII complex would indicate more definitively how the local environment shifts the site energies to produce the variation within and between clusters which results in the directional pathways of energy flow.

In extending these design principles to artificial light harvesting systems, delocalized excited states could be applied in synthetic systems to facilitate ultrafast relaxation and more robust energy transfer between light harvesting complexes. The delocalization of the excited state wave functions plays an important role in inter- and intracomplex energy flow by producing multistep relaxation pathways which effectively channel energy absorbed by many states to the exit states and then to nearby pigment protein complexes. The highly specific molecular interactions and local environment of each site that determine the photosynthetic relaxation pathway could be applied in synthetic devices to optimize their quantum efficiency.

**Acknowledgment.** The authors thank Gregory S. Engel for helpful discussions. This work was supported by Grant No. DE-AC03-76SF000098 from the Chemical Sciences, Geosciences and Biosciences Division, Office of Basic Energy Sciences, Office of Science, U.S. Department of Energy to G.R.F. N.S.G. acknowledges support from a Glenn T. Seaborg Fellowship from LBNL.

**Supporting Information Available:** The full LHCII monomer Hamiltonian used in this work and a description of the fitting methodology is provided in the Supporting Information. This material is available free of charge via the Internet at <http://pubs.acs.org>.

## References and Notes

- (1) Blankenship, R. E. *Molecular mechanisms of photosynthesis*; Blackwell Science: Oxford; Malden, MA, 2002.
- (2) Nield, J.; Barber, J. *Biochim. Biophys. Acta, Bioenerg.* **2006**, 1757, 353.
- (3) Adolphs, J.; Renger, T. *Biophys. J.* **2006**, 91, 2778.
- (4) Frahmcke, J. S.; Walla, P. *J. Chem. Phys. Lett.* **2006**, 430, 397.
- (5) Liu, Z. F.; Yan, H. C.; Wang, K. B.; Kuang, T. Y.; Zhang, J. P.; Gui, L. L.; An, X. M.; Chang, W. R. *Nature* **2004**, 428, 287.
- (6) Standfuss, R.; van Scheltinga, A. C. T.; Lamborghini, M.; Kuhlbrandt, W. *EMBO J.* **2005**, 24, 919.
- (7) Remelli, R.; Varotto, C.; Sandona, D.; Croce, R.; Bassi, R. *J. Biol. Chem.* **1999**, 274, 33510.
- (8) Novoderezhkin, V. I.; Palacios, M. A.; van Amerongen, H.; van Grondelle, R. *J. Phys. Chem. B* **2005**, 109, 10493.
- (9) van Amerongen, H.; Valkunas, L.; van Grondelle, R. *Exciton Dynamics. Photosynthetic excitons*; World Scientific: Singapore; River Edge, N.J., 2000; Ch. 8.
- (10) van Grondelle, R.; Novoderezhkin, V. I. *Phys. Chem. Chem. Phys.* **2006**, 8, 793.
- (11) Rogl, H.; Schodel, R.; Lokstein, H.; Kuhlbrandt, W.; Schubert, A. *Biochemistry* **2002**, 41, 2281.
- (12) Agarwal, R.; Krueger, B. P.; Scholes, G. D.; Yang, M.; Yom, J.; Mets, L.; Fleming, G. R. *J. Phys. Chem. B* **2000**, 104, 2908.
- (13) Palacios, M. A.; Standfuss, J.; Vengris, M.; van Oort, B. F.; van Stokkum, I. H. M.; Kuhlbrandt, W.; van Amerongen, H.; van Grondelle, R. *Photosynth. Res.* **2006**, 88, 269.
- (14) Salverda, J. M.; Vengris, M.; Krueger, B. P.; Scholes, G. D.; Czamoleski, A. R.; Novoderezhkin, V.; van Amerongen, H.; van Grondelle, R. *Biophys. J.* **2003**, 84, 450.
- (15) Georgakopoulou, S.; van der Zwan, G.; Bassi, R.; van Grondelle, R.; van Amerongen, H.; Croce, R. *Biochemistry* **2007**, 46, 4745.
- (16) Gibasiewicz, K.; Rutkowski, M.; Van Grondelle, R. *Photosynthetica* **2009**, 47, 232. Pieper, J.; Ratsep, M.; Irrgang, K. D.; Freiberg, A. *J. Phys. Chem. B* **2009**, 113, 10870.
- (17) Jonas, D. M. *Annu. Rev. Phys. Chem.* **2003**, 54, 425.
- (18) Brixner, T.; Stenger, J.; Vaswani, H. M.; Cho, M.; Blankenship, R. E.; Fleming, G. R. *Nature* **2005**, 434, 625.
- (19) Zigmantas, D.; Read, E. L.; Mancal, T.; Brixner, T.; Gardiner, A. T.; Cogdell, R. J.; Fleming, G. R. *Proc. Natl. Acad. Sci. U.S.A.* **2006**, 103, 12672.
- (20) Caffarri, S.; Croce, R.; Breton, J.; Bassi, R. *J. Biol. Chem.* **2001**, 276, 35924.
- (21) Brixner, T.; Mançal, T.; Stiopkin, I. V.; Fleming, G. R. *J. Chem. Phys.* **2004**, 121, 4221.
- (22) Brixner, T.; Stiopkin, I. V.; Fleming, G. R. *Opt. Lett.* **2004**, 29, 884.
- (23) Novoderezhkin, V. I.; Palacios, M. A.; van Amerongen, H.; van Grondelle, R. *J. Phys. Chem. B* **2004**, 108, 10363.
- (24) Peterman, E. J. G.; Pullerits, T.; van Grondelle, R.; van Amerongen, H. *J. Phys. Chem. B* **1997**, 101, 4448.
- (25) Zhang, W. M.; Meier, T.; Chernyak, V.; Mukamel, S. *J. Chem. Phys.* **1998**, 108, 7763. Yang, M. N.; Fleming, G. R. *J. Chem. Phys.* **2003**, 119, 5614.
- (26) Linnanto, J.; Martiskainen, J.; Lehtovuori, V.; Ihälainen, J.; Kananavicius, R.; Barbato, R.; Korppi-Tommola, J. *Photosynth. Res.* **2006**, 87, 267.
- (27) Ernst, R. R.; Bodenhausen, G.; Wokaun, A. *Principles of Nuclear Magnetic Resonance in One and Two Dimensions*; Oxford Science Publications: Oxford, 1987.
- (28) Cheng, Y. C.; Fleming, G. R. *J. Phys. Chem. A* **2008**, 112, 4254.
- (29) Read, E. L.; Engel, G. S.; Calhoun, T. R.; Mancal, T.; Ahn, T. K.; Blankenship, R. E.; Fleming, G. R. *Proc. Natl. Acad. Sci. U.S.A.* **2007**, 104, 14203.
- (30) Calhoun, T. R.; Ginsberg, N. S.; Schlau-Cohen, G. S.; Cheng, Y.-C.; Ballottari, M.; Bassi, R.; Fleming, G. R. *J. Phys. Chem. B* **2009**, in press.
- (31) Rivadossi, A.; Zucchelli, G.; Garlaschi, F. M.; Jennings, R. C. *Photochem. Photobiol.* **2004**, 80, 492.
- (32) Lee, H.; Cheng, Y. C.; Fleming, G. R. *Science* **2007**, 316, 1462.
- (33) Wen, J.; Zhang, H.; Gross, M. L.; Blankenship, R. E. *Proc. Natl. Acad. Sci. U.S.A.* **2009**, in press.
- (34) Poliakov, E. Y.; Chernyak, V.; Tretiak, S.; Mukamel, S. *J. Chem. Phys.* **1999**, 110, 8161.
- (35) Scholes, G. D. *Annu. Rev. Phys. Chem.* **2003**, 54, 57.
- (36) Scholes, G. D.; Jordanides, X. J.; Fleming, G. R. *J. Phys. Chem. B* **2001**, 105, 1640.
- (37) Muh, F.; El-Amine Madjet, M.; Adolphs, J.; Abdurahman, A.; Rabenstein, B.; Ishikita, H.; Knapp, E.-W.; Renger, T. *Proc. Natl. Acad. Sci. U.S.A.* **2007**, 104, 16862.